# SUPPORTING INFORMATION

## Graphene Translucency and Interfacial Interactions in The Gold/Graphene/SiC System

Mario Caccia,[1] Donatella Giuranno,[2] José M. Molina-Jorda,[1] Mónica Moral,[3] Rafal Nowak,[4] Enrica Ricci,[2] Natalie Sobczak,[4] Javier Narciso,[1] Javier Fernández Sanz[3]*

[1]*Departamento de Química Inorgánica e Instituto Universitario de Materiales de Alicante, Universidad de Alicante, Alicante (Spain)*

[2] *National Research Council (CNR), Institute of Condensed Matter Chemistry and Energy Technologies (ICMATE), Genoa (Italy)*

[3]*Departamento de Química Física, Universidad de Sevilla, Sevilla (Spain)*

[4]*Foundry Research Institute, Krakow (Poland)*

*E-mail: sanz@us.es

**S.1. Wetting tests: experimental device and procedure**

The Center for High Temperature Studies of Liquid Metals and Alloys at the Foundry Research Institute, Krakow centre has a complex experimental measurements capillary to high temperature, which among its many possible configurations of work, one that conforms to the requirements of this study. The complex is currently the only one in the world who qualifies to perform this in situ study. Among the job opportunities of these facilities include (1):

- Vacuum chamber for initial sample preparation, in which vacuum can be preheated to 473K.
- Chamber of ultra-high vacuum (UHV, $10^{-5}$ Pa) with the possibility of transporting the sample from one chamber to another using a manipulator for samples of various sizes and geometries.
- Analytical chamber containing Auger / XPS spectrometer for surface characterization, both before and after heat treatment and an ion gun for surface cleaning of samples.
- A "portable" vacuum chamber for collection and storage of samples after testing.

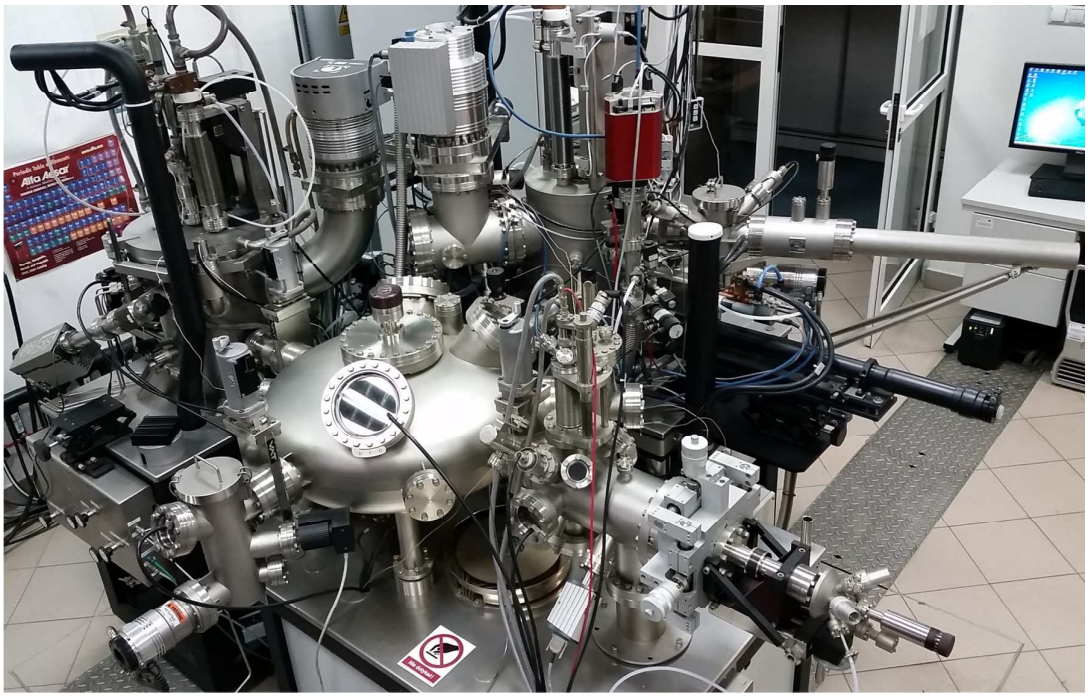

**Figure S1**. Photograph of experimental complex for investigation of high temperature phenomena, between liquid metals and solid substrates (wetting behaviour, contact angle measurements, spreading, adhesion).

- Experimental chamber to work at high temperature (up to 2300 K), with both solid and molten materials. This camera features:
  - Heating elements, and moving screens (vertically).
  - Additional windows for observation and recording.

- Mass spectrometer quadrupole coupled to the real-time measurement of the chemical composition of vacuum.
- Capillary with vertical movement for purification procedures to remove molten metal or metal drop after sessile drop test.
- A manipulator below the substrate shows that seeks to be "sandwiched drop" or add alloying and form alloys in situ under vacuum.
- Temperature control in real time using 4 thermocouples.
- Possibility of maintaining a gas flow or atmosphere with a controlled flow or a certain pressure.
- High-resolution digital camera with an engraving system for real-time image acquisition during tests.

Figure S1 shows a photograph of the above-described equipment to be used for high temperature studies of interaction between liquid metals and solid substrates.

**S.2. Contact angle measurements and results**

The wetting behavior of liquid gold on SiC-supported graphene with variable thickness (from 1 to more than three graphene layers), was evaluated by contact angle measurements using the sessile drop method (2).

As already mentioned in the previous section, two different experimental procedures were applied to obtain the liquid gold (Au) sessile drop on the selected substrate: by "classical" contact heating (CH) and by dispensed drop (DD). In particular, in this last case was possible to dispense a fresh liquid Au drop on the SiC and HOPG substrates *in situ* previously treated by an $Ar^+$ ion sputtering in order to remove native oxide films.

The wetting experiments performed, and their testing parameters are summarized in Table S1.

**Table S1**. Summary of wetting experiments performed, their testing parameters and experimental procedure applied.

| System | Testing parameters | Experimental procedure |
|---|---|---|
| Au/SiC | 1373 K / Ar | DD |
| Au/SiC | 1373 K / Vacuum | DD |
| Au/ML/SiC | 1373 K / Ar | CH |
| Au/ML/SiC | 1373 K / Vacuum | CH |
| Au/BL/SiC | 1373K / Ar | CH |
| Au/BL/SiC | 1373 K / Vacuum | CH |
| Au/FL/SiC | 1373 K / Ar | CH |
| Au/FL/SiC | 1373 K / Vacuum | CH |
| Au/HOPG | 1373 K / Ar | DD |
| Au/HOPG | 1373 K / Vacuum | DD |

During each run, images of the drop/substrate couples were recorded (100 fps) using a high-speed MC1310 camera with a resolution of 1024x768 pixels and off-line processed by an ad-hoc developed software, ASTRAview, in order to calculate static (advancing) contact angle value and the dimensions (height and base diameter) of each sessile drop.

In Figure 2, the contact angle of liquid Au/4H-SiC curve vs. time obtained by dispensing a liquid Au drop at a constant temperature of T = 1373 K under an Ar atmosphere is shown. As it can be seen, after the deposition of the liquid Au drop on the 4H-SiC substrate, *in situ* previously treated by an $Ar^+$ ion sputtering, the equilibrium contact angle value of $\theta \approx 142°$ was reached in less than 90 s. The same procedure was applied to study the contact angle behavior of Au/4H-SiC couple under a dynamic vacuum of $P_{tot} \approx 10^{-3}$ Pa. As already reported, a final contact angle value of $\theta \approx 139°$ was observed.

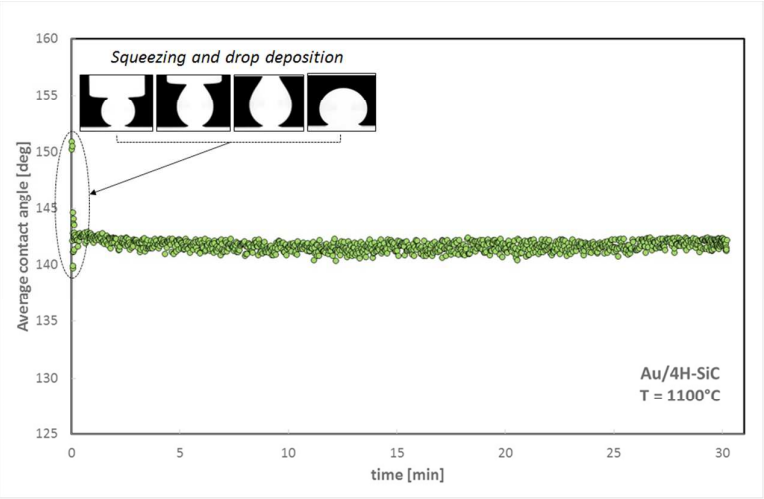


**Figure S2**. Contact angle of Au dispensed drop on 4H-SiC substrate as a function of time at constant temperature of T = 1373K under a high purity Ar atmosphere

As discussed, the contact angle values obtained for Au/4H-SiC under an Ar atmosphere and under a vacuum are in very good agreement with the available literature data (3). Here following, the Table presents an overview of the final contact angle values measured during the wetting experiments.

As a general comment, the intrinsic precision of the contact angle data was of the order of 0.1-0.4°, however, possible optical distortions due to the high temperature involved lead to uncertainties in the measured profiles that suggest a more conservative final contact-angle accuracy of the order of ±2° (4).

**Table S2**. Final contact angle values and standard deviation (image-to-image scatter) estimated on the images captured during last 60 s of each run.

| System | Testing parameters | Final Contact angle | Standard deviation |
|---|---|---|---|
| Au/SiC | 1373 K / Ar | 142 | 0.3 |
| Au/SiC | 1373 K / Vacuum | 139 | 0.3 |

| | | | |
|---|---|---|---|
| Au/ML/SiC | 1373 K / Ar | 132.5 | 0.4 |
| Au/ML/SiC | 1373 K / Vacuum | 130 | 0.4 |
| Au/BL/SiC | 1373 K / Ar | 129.5 | 0.3 |
| Au/BL/SiC | 1373 K / Vacuum | 128 | 0.3 |
| Au/FL/SiC | 1373 K / Ar | 126 | 0.2 |
| Au/FL/SiC | 1373 K / Vacuum | 126 | 0.1 |
| Au/HOPG | 1373 K / Ar | 125.5 | 0.2 |
| Au/HOPG | 1373 K / Vacuum | 125 | 0.3 |

**S.2.1 ASTRAview: from image analysis to contact angle values**

**ASTRA** (Automatic Surface Tension Real Time Acquisition) (5) is an experimental methodology and an integral software, developed in a LABview® environment (**ASTRAview©**), to get and process captured images, to extract drop shape profiles and to determine surface and interfacial tension, surface area, contact angle values, as well as geometrical parameters (height, base diameter, drop volume, etc.) of a liquid sessile/pendant drop. Due to its high performances in terms of time of acquisition and reliability, it is possible, in real time, to analyse up to 20 drop profiles per second, having access to dynamic measurements over large time scale. ASTRAview is currently used both in the CNR-ICMATE and FRI laboratories. For the acquisition and processing of the drop image, the NI-IMAQ system is used (National Instruments Milano, Italy). It consists of an interface processor connected to a personal computer, which digitises each frame coming from a B/W camera into 1024x768 image points (pixels), assigning to each pixel a grey level value ranging from 0 (black) to 255 (white). In this way, the image frames are digitised into 1024x768 and treated as a matrix whose $P_{ij}$ element, on choosing a Cartesian reference compatible with the standard matrix notation, is the average grey level of the pixel with its bottom-right comer at the coordinate point (i,j). The images coming from the camera can be processed in real time, or stored in order to be processed later (off-line). In determining reliable interfacial properties, ASTRA experimental methodology flows through four sequential modules:

-*Set procedure*: the images acquisition frequency can be set (only enabled under real-time acquisition data) and the arbitrary selection of the interesting interfacial properties and geometrical parameters can be done.

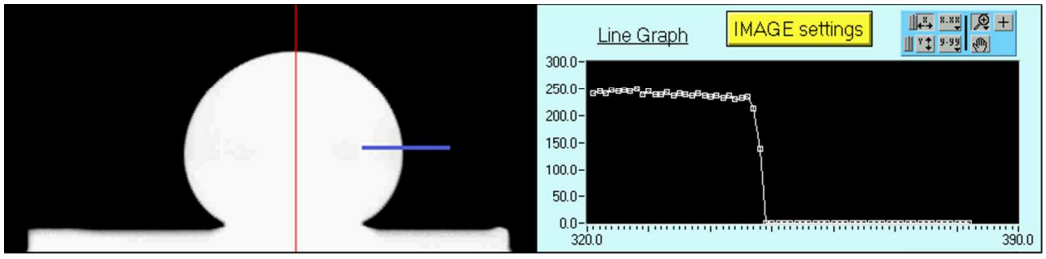


**Figure S3**. Au drop/4H-SiC substrate gray-scale image and the corresponding gray level profile

-*Set view*: the image quality is evaluated, and the reference dimension is introduced (to calculate reliable surface tension data and drop dimensions). As extensively discussed by Eustathopoulos et al. (4) and Sobczak et al. (6), with the aim to increase the accuracy of experimental data, a sharp drop/substrate image with well-demarcated boundaries is crucial. The gray-scale image consists of a white foreground (grey level ≈ 250) in a dark background (grey level = 0). The image quality is estimated by a line scan analysis of pixels intensities crossing the drop profile. As it can be seen in Figure S3, the drop edge is detected with an uncertainty of 1 pixel.

-*Set experiment*: it is possible to set the position of reference lines (Figure S4) and to process the drop/substrate profile to obtain contact angle, surface tension and drop dimensions values.

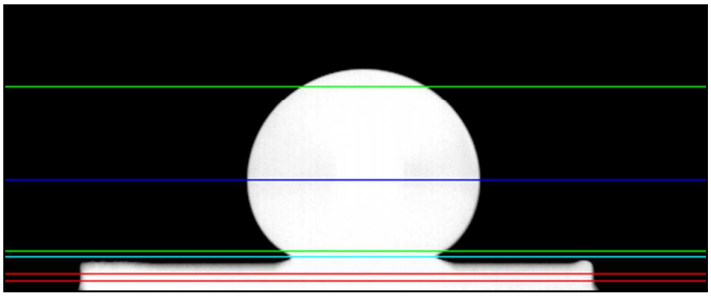

**Figure S4**. Au drop/4H-SiC substrate gray-scale image and the ASTRAview reference lines.

As it can be seen in Figure 4, the triple line (TL) is easily identified by the light blue baseline. The portions of profile between baseline and blue line (set at the maximum drop diameter), baseline and the highest green line are processed to calculate contact angle and drop dimensions values, respectively, with a number of coordinate points used large enough to warrant a sufficient statistical accuracy. On the contrary, the portion of drop profile between the two green lines is used to obtain surface tension data. Reliable surface tension data and drop dimensions are obtained by an accurate determination of the reference dimension of the system used. It is essential for deriving the real drop profile coordinates. It is identified by the software between the red lines knowing the actual dimension of the substrate as a function of temperature.

-*Acquisition* module: each drop/substrate image is scanned in horizontal and vertical directions and the edge position is determined as the point where the absolute variation in the grey level is a maximum or at the threshold value imposed to optimize the fitting of the drop. This module also acquires the dimensions of the substrate to establish the reference dimension. Finally, from the drop shape analysis is possible to obtain the interfacial properties values and drop dimensions already mentioned.

Surface tension and contact angle values are calculated from the drop profile using the non-linear regression method proposed by Maze and Burnet (7). Essentially, the method consists of a non-linear regression procedure in which a number of arbitrarily selected coordinate points on the drop profile are fitted by a calculated Laplacian curve and the best fit is obtained by optimizing two parameters: apex radius and shape factor.

The advantage of this method is that the measured drop profile is described by a set of coordinate points. To start the fitting procedure, the algorithm needs reasonable values of drop shape factor and drop size in order to help the convergence of the calculated Laplacian curve to the reconstructed drop profile. Maze and Burnet algorithm is not suitable to calculate surface tension and contact angle for sessile drops strongly influenced by gravity. In fact, liquid drops of low surface tension end to flatten near the apex, and the difficulty to reconstruct the drop profile by a set of coordinate points near the apex region may cause a large error. To overcome this limit, in approaching the apex region, ASTRAview converts the drop edge detection method from horizontal scanning to vertical one.

In order to assess the validity of ASTRA methodology and to identify possible sources of errors, several tests were previously performed by evaluating the accuracy in determining surface tension value (more sensitive respect to contact angle) of liquid Au as a function of temperature by sessile and pendant drop methods: as for example, the accuracy of the drop edge detection was increased by optimizing the grey-level transition allowing to rebuild the drop profile close to the real one. In addition, as suggested by Eustathopoulos et al. (4) and Sobczak et al. (6) in order to increase the reproducibility, all the possible "external factors" (optical distortions phenomena, uncertainty in temperature measurements, etc.) affecting the correct determination of surface tension and contact angle values were deeply evaluated. In particular, for contact angle values an error bar less than ± 2° was estimated.

**S.3 Characterization of substrates prior and ulterior wetting tests**

**S.3.1 Substrates**

7x7 $mm^2$ square 4H-SiC substrates coated with graphene were purchased from GraphenSiC (8). Substrates are 4H single crystals with an orientation of 0001 and a deviation from the 0001 plane of 0.25º (due to cutting). Substrates with three different graphene thicknesses were used: monolayer graphene (ML), bilayer graphene (BL) and few layer graphene (FL, 3-4 layers). The supplier guarantees 100% coverage of the SiC substrate with graphene. ML/SiC substrate is dominated by monolayer graphene coverage, with <15% bilayer islands. BL/SiC substrate has over 50% coverage of bilayer graphene with trilayer islands. FL/SiC substrate has over 50% coverage of trilayer graphene with areas of bilayer and four layers.

**Pre-wetting tests surface characterization**

The different substrates were characterized in the as-received condition using Raman spectroscopy (9) and Auger spectroscopy as a contrast technique (10) to evaluate the number of graphene layers. Surface chemistry was studied using X-ray photoelectron spectroscopy.

Raman spectra were obtained using He laser (633 nm) and Auger differential spectra were obtained from the C KLL spectra of each substrate. Figure S5 shows representative Raman and differential Auger spectra obtained for the different substrates used.

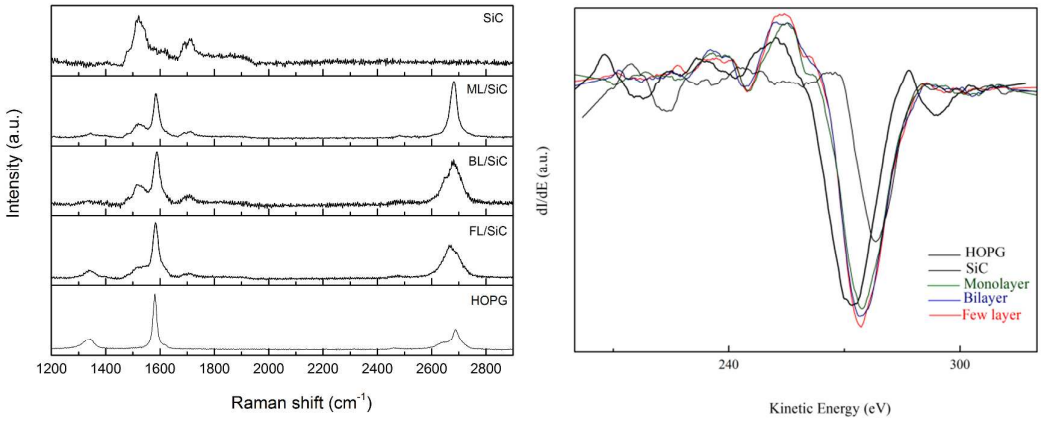


**Figure S5**. Raman spectra and differential Auger spectra of the different substrates.

The substrates containing graphene layers exhibit the 3 most characteristic bands of graphitic materials, namely the D (1320 $cm^{-1}$), G (1580 $cm^{-1}$) and G' or 2G (2700 $cm^{-1}$) bands. The intensity relationship between the bands was evaluated and it is reported in Table S3. The $I_{2G}/I_G$ ratio is related to the number of graphene layers while the $I_D/I_G$ ratio provides information on the density of defects within the graphitic layers. The $I_{2G}/I_G$ values observed coincide with the reported values in literature for the different number of graphene layers, and the low $I_D/I_G$ values indicate a low density of initial defects (11), being the ML/SiC sample the one with less defects.

**Table S3.** $I_{2D}/I_G$ and $I_D/I_G$ ratios for the different substrates.

| Substrate | $I_{2D}/I_G$ | $I_D/I_G$ |
|---|---|---|
| ML/SiC | 1.21 | 0.29 |
| BL/SiC | 0.90 | 0.34 |
| FL/SiC | 0.65 | 0.35 |

The differential Auger spectrum of uncoated 4H-SiC shows a characteristic band at a kinetic energy of around 380 eV. A shift towards lower kinetic energy is observed for the coated substrates with increasing number of graphene layers, thus confirming the increasing thickness of graphene estimated with Raman spectroscopy.

Figure S6 shows the C1s and O1s spectra for the FL/SiC, HOPG and a pure SiC substrates. The band observed at 284.6 eV is attributed to $sp^2$ configuration of carbon atoms, and it is present in all samples. The band at lower binding energy, around 283.5 eV is attributed to the C-Si bond in SiC and is present in the SiC uncoated substrate and in the FL/SiC substrate indicating that the depth of analysis is deeper than the few layers of graphene. The two bands observed at 285.5 and 286.4 eV in the FL/SiC sample are associated to the buffer layer between graphene and SiC (11). HOPG and SiC present two bands at higher binding energy (286.5 and 288.5-289 eV), which are usually associated to oxygen-containing molecules adsorbed at the surface. The lower binding energy is usually associated to the C-O bond, while the band at higher binding energy is commonly associated to the C=O bond (12-14). The band at 286.4 in the FL/SiC sample could be overlapped with the C-O band. The O1s spectra of all

samples confirms the presence of such groups which are depicted as two bands at 532.5 and 534 eV, being the latter usually associated to adsorbed molecular water and oxygen surface groups containing a C=O bond. Figure S7 shows the Si2p3/2 spectra for the FL/SiC and the SiC samples. Both samples show a band around 102 eV that corresponds to Si-Si bond. The FL/SiC sample shows a band at a binding energy of 101 eV, 1 eV higher than the Si-C band shown in pure SiC. This displacement may be attributed to the buffer layer that stands between graphene and SiC which consists of C atoms bonded to SiC with a different bond length than in pure SiC. Finally, the pure SiC sample shows the presence of Si-O bonds that correspond to surface oxygen groups.

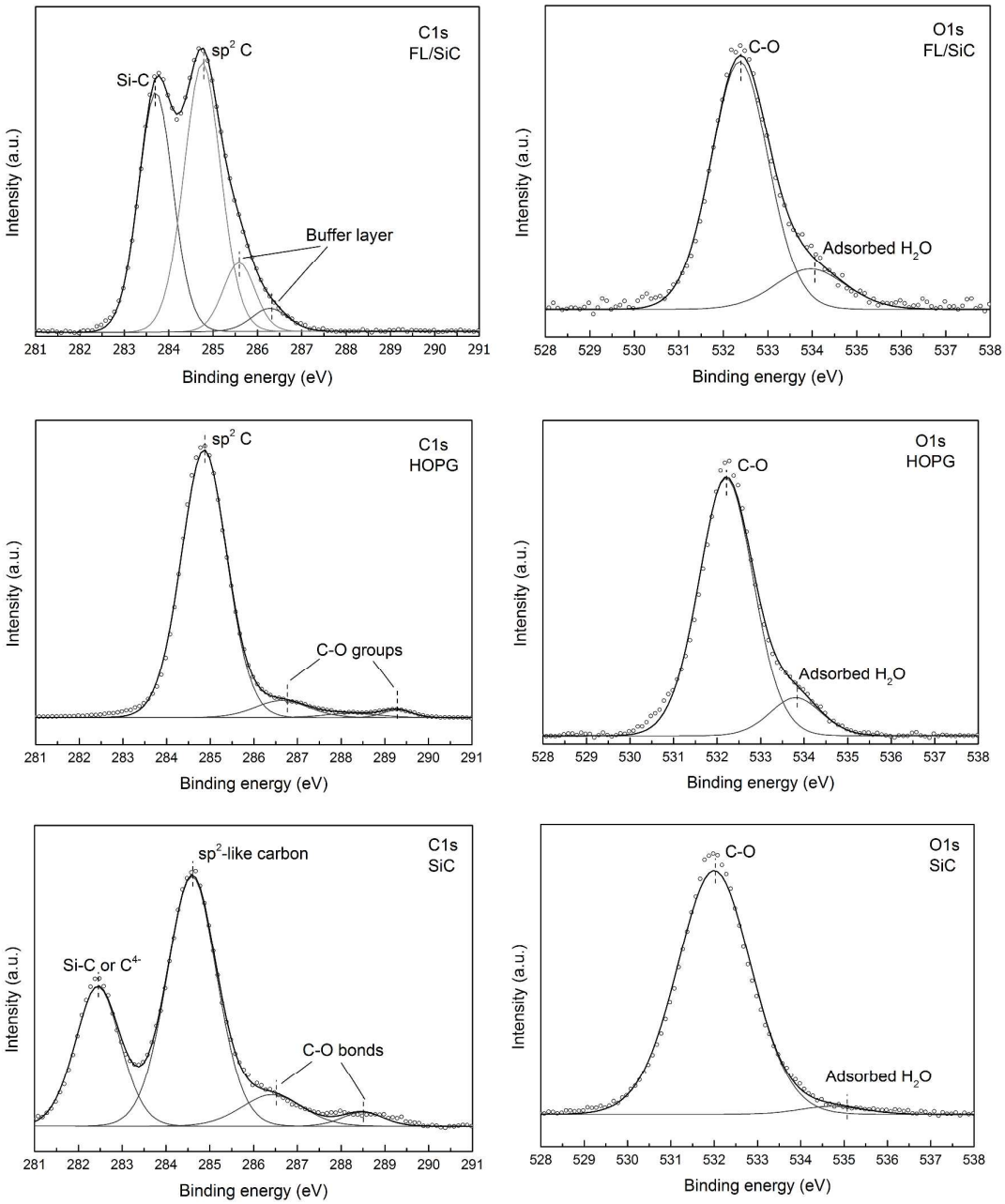


**Figure S6**. C1s and O1s spectra of FL/SiC (top), H.O.P.G. (middle) and SiC (bottom).

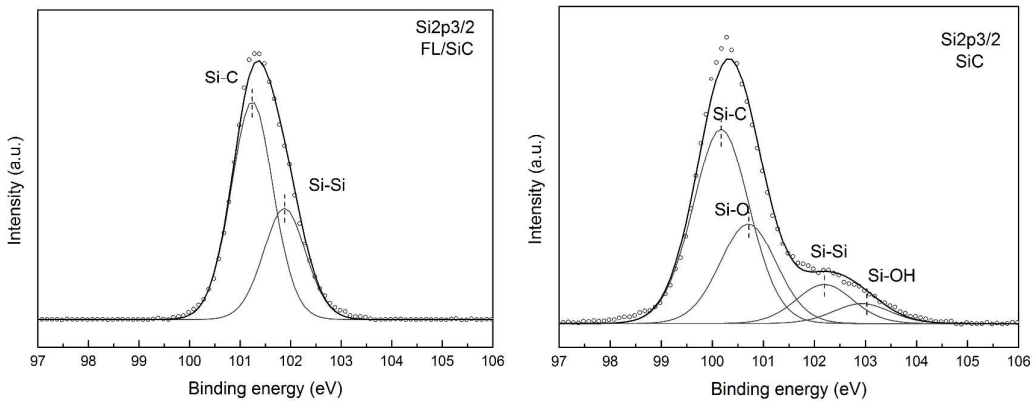


**Figure S7**- Si2p3/2 spectra of few layer graphene on SiC (left), and a SiC Lely single crystal (right).

**During-wetting tests surface characterization**

During the first stage of wetting tests performed under Ar atmosphere, the samples were heated until 973 K under high vacuum ($10^{-3}$ Pa) to remove adsorbed species form the surface. After reaching 973 K Ar was introduced inside the experimental chamber. The chemistry of the surface of the substrates was evaluated using a mass spectrometer coupled to the experimental chamber during heating. The desorption profiles obtained for the ML/SiC, the BL/SiC and the FL/SiC samples are shown in Figure S8. Water, CO and $CO_2$ are the main gases desorbing from the samples. Because water desorption occurred only at low temperatures (< 423 K) it is assumed it corresponds to moisture and weakly bonded water and will be disregarded in this analysis.

As observed in the XPS analysis (Pre-wetting test characterization), oxygen surface groups are present in all samples. Depending on their nature these groups decompose at different temperatures as CO or $CO_2$ (15). CO and $CO_2$ desorption begins at the same temperature (around 650 K) and evolves during heating as the different groups decompose. In all samples, the low temperature desorption of $CO_2$ may be attributed to carboxylic groups (consistent with the band observed at XPS around 286 eV in the C1s spectrum and at 531 eV in the O1s spectrum), while at temperatures above 873 K, desorption of lactone groups may be occurring (consistent with the 534 eV band observed for the O1s spectrum). Low temperature desorption of CO can be attributed to the simultaneous desorption of CO and $CO_2$ caused by decomposition of anhydride groups, while CO desorption at higher temperatures may indicate the presence of ether or carbonyl groups (16). While the desorption of oxygen-containing groups can generate defects in the graphene layers, these results indicate that the surface of the samples was as clean as possible before the wetting experiments were performed. The effects that desorption of these groups might have on the structure of the graphene layers and the wetting behavior will be discussed in the next sections.

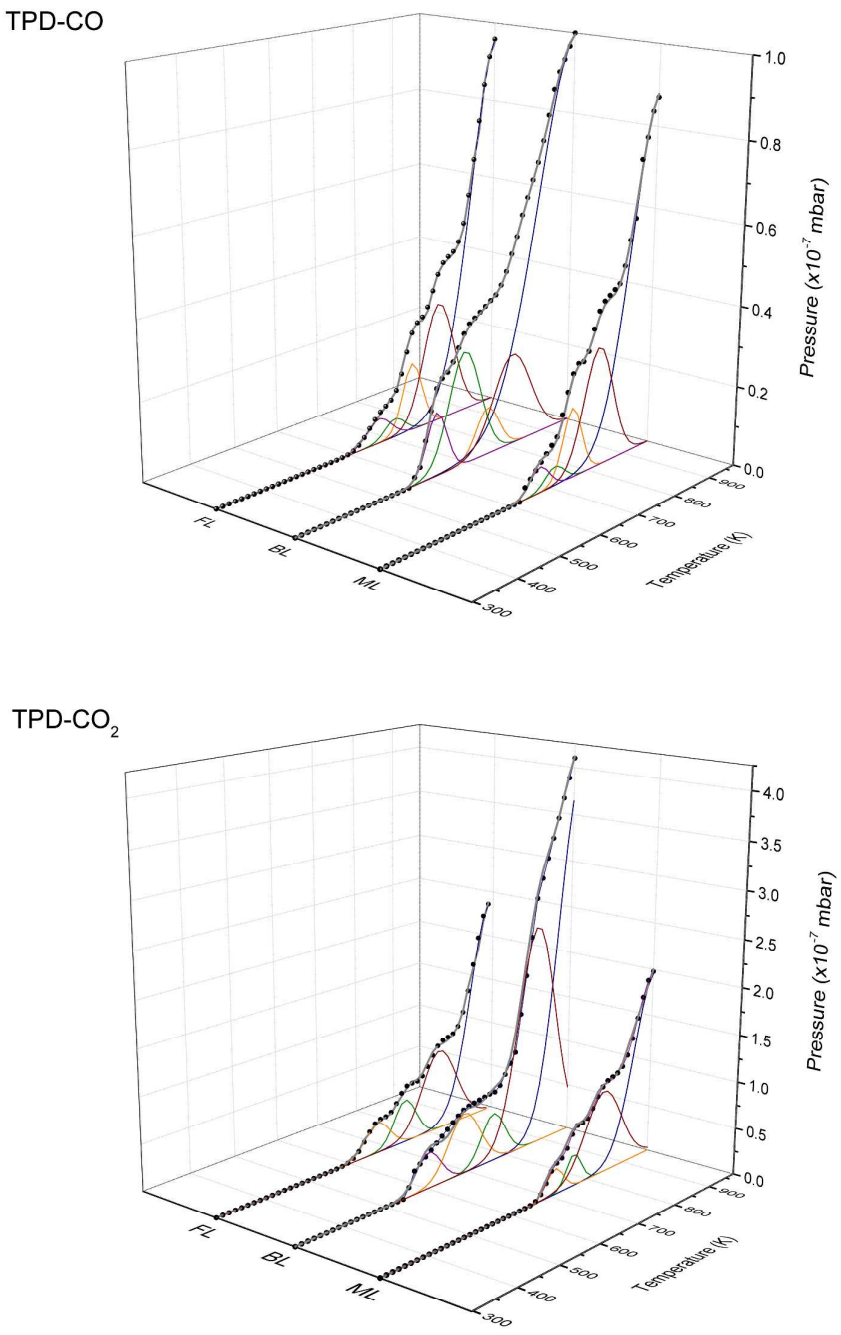


**Figure S8**. CO and $CO_2$ desorption profiles obtained during heating of the samples until 973 K under HV ($10^{-3}$ Pa). A deconvolution of the profiles has been done to identify the different surface groups. Groups desorbing at the same temperature have been marked using the same color.

**Post-wetting experiments surface characterization**

After wetting experiments, the surface of the substrates both, around and below, the drop of Au, were analyzed using Raman spectroscopy to evaluate the structural changes in graphene. To remove Au without disrupting the underlying surface, an in-house made device (see Figure S9) was used to dissolve

Au droplets by alloying with Hg. The device minimizes the contact between the substrate and Hg. Table S4 summarizes the changes in the $I_{2D}/I_G$ and the $I_D/I_G$ ratios measured on the substrate surrounding the Au drop.

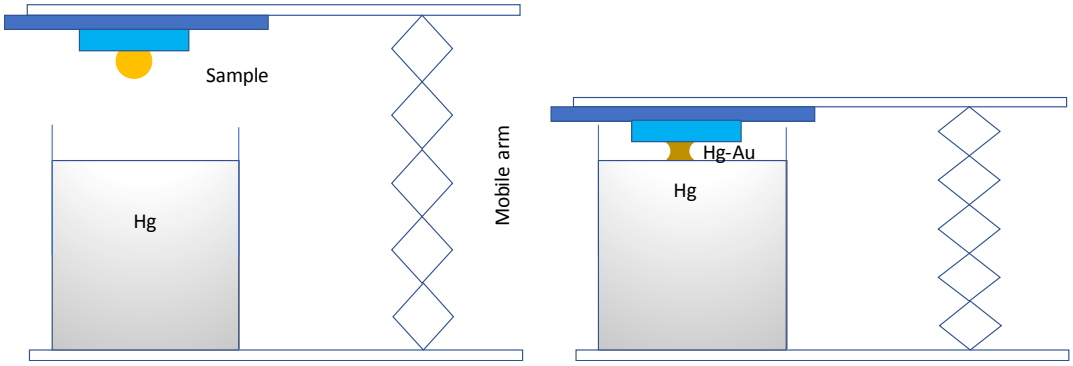


**Figure S9**. Schematic representation of the in-house made device used for removing Au droplets by alloying. Initial situation (left side). Alloying and dissolution of gold (right side).

As aforementioned, the density of defects can be evaluated with the ratio $I_D/I_G$. For the ML/SiC sample tested under Ar atmosphere, $I_D/I_G$ changes from 0.29 to 0.71, indicating that the number of defects has increased, even though the value remains in the so called "low defect density" regime (17). For BL/SiC and FL/SiC, there is no significant increase in the $I_D/I_G$ value. The desorption of oxygen surface groups, as well as small remaining amounts of oxygen in the atmosphere, can generate defects in graphene layers. The mass spectroscopy and the XPS analysis showed the presence of oxygen surface groups in all samples, and equilibrium calculations indicate that the oxygen partial pressure ($pO_2$) in the chamber during experiments was $10^{-19}$ Pa under Ar, and $10^{-18}$ Pa under vacuum. These two oxygen sources can justify the increase in the disorder of the graphene layers observed, as defects (mainly vacancies) are formed by C atom removal. It seems, though, that defects generated are negligible when more than one graphene layer is present or that these defects are being regenerated from the underlying layers. Atom vacancies present the lowest migration energy among the possible defects in graphene (18), which means that at the experimental temperature it is possible to have these defects migrating to regenerate the $sp^2$ structure of graphene. There is also a significant change in the $I_{2D}/I_G$ value for the ML/SiC sample. At first glance, this could indicate that graphene layers are growing during the experiment and that BL and FL islands are being formed. However, a change in the $I_{2D}/I_G$ could also indicate a distortion of the graphene layer by rotation, which would also modify the $I_D/I_G$ value. The shape of the 2D band is slightly less symmetrical than for the as received substrate (see Figure S10), which suggests a growth in the graphene layer number. In the case of the BL/SiC sample, as part of the initial surface of the substrate is covered in trilayer islands, it is hard to evaluate if there was a growth in the number of graphene layers or even a distortion of the surface just by analyzing the $I_{2D}/I_G$. Nevertheless, since there are no changes in the $I_D/I_G$ value, it could be concluded that no distortions are taking place.

**Table S4**. Raman spectroscopy analysis of the substrate surrounding the drop. The values provided are the average of 3 different measurements in different points.

| Sample | Experimental conditions | $I_{2D}/I_G$ | $I_D/I_G$ |
|---|---|---|---|
| ML/SIC | As received | 1.21 | 0.29 |
| ML/SiC | 1373 K / Ar | 0.71 | 0.70 |
| ML/SiC | 1373 K / vacuum | 0.51 | 0.45 |
| BL/SiC | As received | 0.90 | 0.30 |
| BL/SiC | 1373 K / Ar | 0.57 | 0.35 |
| BL/SiC | 1373 K / vacuum | 0.50 | 0.35 |
| BL/SiC | 1373 K / vacuum | 0.54 | 0.39 |
| FL/SIC | As received | 0.65 | 0.35 |
| FL/SiC | 1373 K / Ar / vacuum | 0.56 | 0.11 |

As for the experiments performed under vacuum atmosphere, the value of $I_{2D}/I_G$ of the ML/SiC sample decreases from 1.21 to 0.51. The value of the $I_D/I_G$ increases slightly from 0.29 to 0.45, showing a value lower than for the experiment under Ar, as expected considering that the $pO_2$ is lower under vacuum. Taking this evidence into account it is possible to state almost unequivocally that more graphene layers have grown during the experiment and that the substrate is now covered with a few layers instead of a monolayer. The same can be observed for the BL sample, although it is more difficult to assure the growth of graphene layers for this sample, which was initially covered with some trilayer islands.

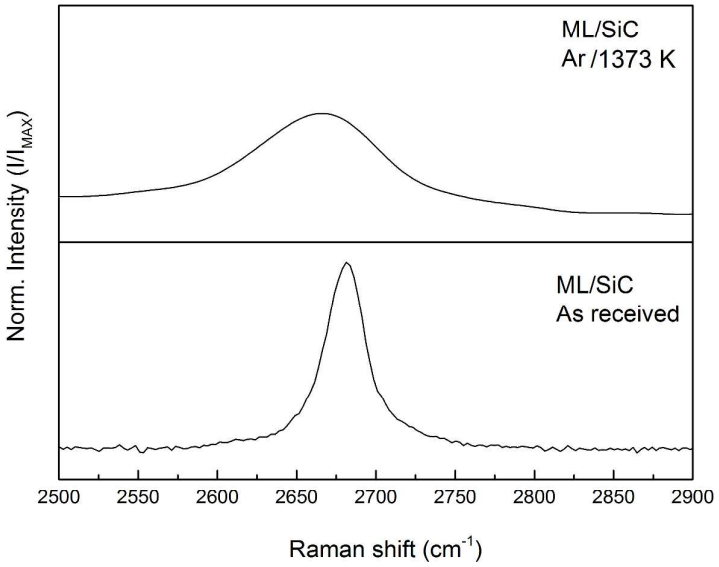


**Figure S10**. 2D band of the Raman spectra of as received ML/SiC sample and the same sample after the wetting test at 1373K under Ar atmosphere.

Raman analysis was also carried out, after removing the Au, in the region below the drop. The $I_{2D}/I_G$ and $I_D/I_G$ values are reported in Table S5. In general, for samples tested under Ar, all samples show a dramatic increase in the $I_D/I_G$ ratio, indicating a great augment of defect density, most likely caused by a distortion in the graphene layers because of the presence of Au that could exert a steric effect hindering the desorption of surface groups and thus generating distortions in the atomic C net. The value of $I_{2D}/I_G$ decreases for all samples indicating either a growth of graphene layers or a severe distortion of the original layers. It is also possible that part of this distortion was originated from the droplet removal process.

For experiments performed under vacuum, there is a slight decrease in the $I_{2D}/I_G$ value for both ML and BL samples, and a small/medium increase in the $I_D/I_G$ value. The cause for the $I_D/I_G$ ratio increase probably has the same origin as for samples tested under Ar. As in the measurements performed around the drop, it seems that during experiments under vacuum graphene layers grow quite homogeneously on the substrate, even under the molten drop of Au.

**Table S5**. Raman spectroscopy analysis of the substrate below the drop after removal with Hg.

| Sample | Experimental conditions | $I_{2D}/I_G$ | $I_D/I_G$ |
|---|---|---|---|
| ML/SIC | As received | 1.21 | 0.29 |
| ML/SiC | 1373 K / Ar | 0.68 | 1.19 |
| ML/SiC | 1373 K / Vacuum | 0.79 | 0.77 |
| BL/SiC | As received | 0.90 | 0.30 |
| BL/SiC | 1373 K / Ar | 0.49 | 1.23 |
| BL/SiC | 1373 K / Vacuum | 0.71 | 0.52 |
| FL/SiC | As received | 0.65 | 0.35 |
| FL/SiC | 1373 K / Ar / Vacuum | 0.59 | 0.95 |

**Dissolution phenomena**

To determine whether dissolution of either C or Si took place during wetting tests, Raman spectroscopy and EDS measurements were performed on selected samples after the wetting tests. Figure S11 shows the Raman spectra obtained on top of the different gold droplets, where no presence of the characteristic bands associated to carbon materials are observed, thus ruling out carbon dissolution.

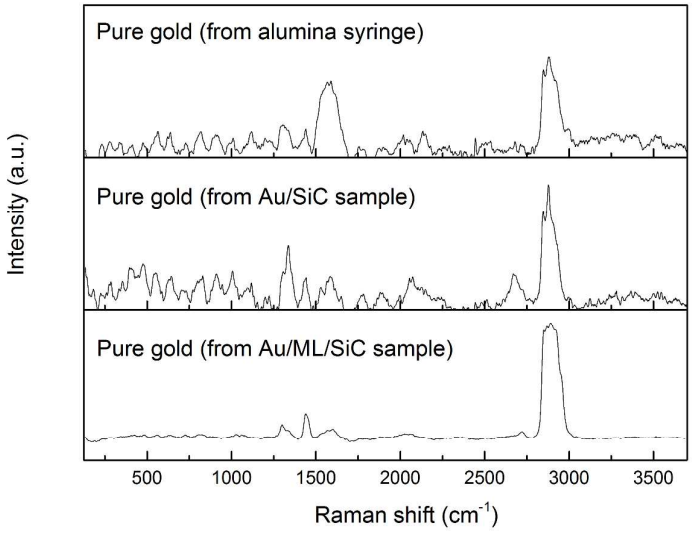


**Figure S11**. Raman spectra obtained on the top of Au droplets recovered from (a) the alumina syringe used for squeezing the metal on the substrates, (b) from the Au/SiC sample, and (c) from the Au/ML/SiC sample.

Figure S12 shows a backscattered electron SEM image of a polished cross-section of the Au/4H-SiC sample. No dissolution of Si is detected from the SiC into the metal neither by visual inspection nor by EDS (see Figure S13). The small roughness observed at the interface is probably a consequence of the polishing procedure, as it is also observed on the SiC outside the drop.

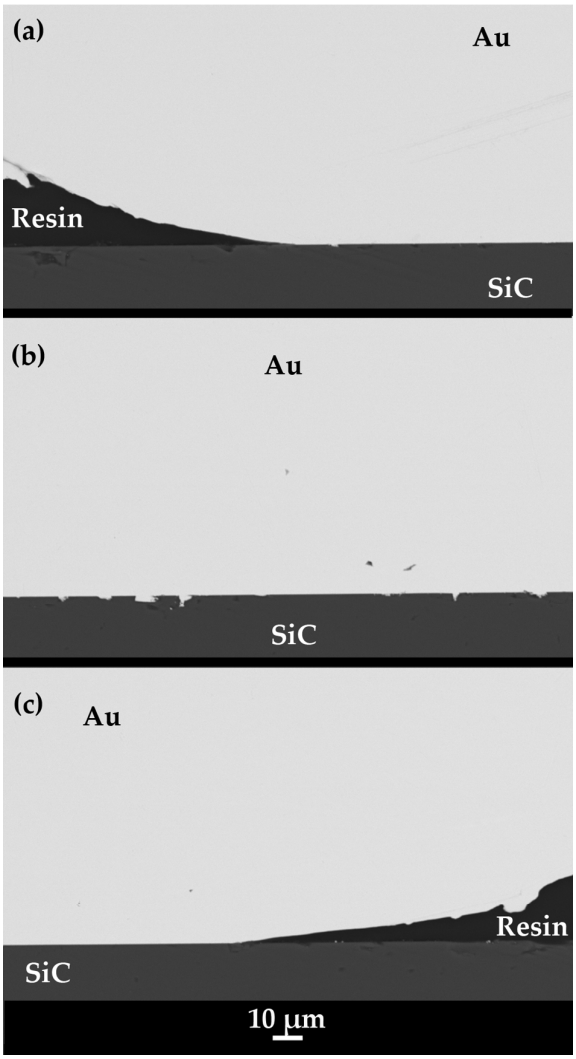


**Figure S12**. Backscattered electron SEM images of the polished cross section of the Au/SiC sample showing the Au/SiC interface at the left triple line (top), the center of the drop (middle) and the right triple line (bottom).

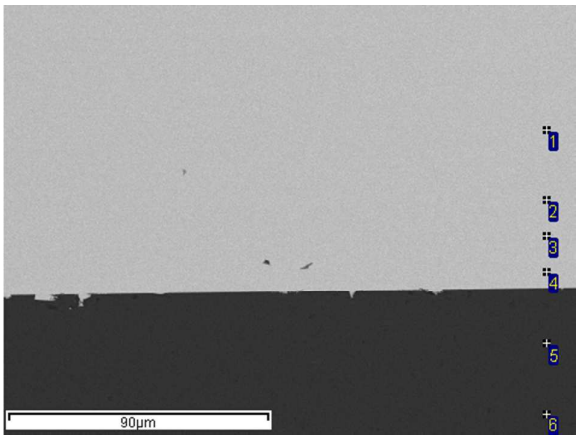


| Spectrum | C | Si | Au |
|---|---|---|---|
| **1** | | | 100 |
| **2** | | | 100 |
| **3** | | | 100 |
| **4** | | | 100 |
| **5** | 53.58 | 46.42 | |
| **6** | 52.84 | 47.16 | |

**Figure S13**. SEM micrograph and EDS analysis (in at%) performed at the center of Au/SiC interface.

**References**


1.- Sobczak, N.; Nowak, R.; Radziwill, W.; Budzioch, J.; Glenz, A. Experimental Complex for Investigations of High Temperature Capillarity Phenomena. *Mater. Sci. Eng. A,* **2008**, *495*, 43-49.

2.- Eustathopoulos, N.; Nicholas, M.G.; Drevet, B. (Eds.) *Wettability at High Temperatures* (Vol. 3). Elsevier Science Ltd.: Oxford, 1999.

3.- Naidich, Y.V.; Zhuravlev, V.; Krasovskaya, N. The Wettability of Silicon Carbide by Au–Si Alloys. *Mater. Sci. Eng. A* **1998**, *245*, 293–299.

4.- Eustathopoulos, N.; Sobczak, N.; Passerone, A.; Nogi, K. Measurement of Contact Angle and Work of Adhesion at High Temperature. *J. Mater. Sci.* **2005**, *40*, 2271-2280.

5.- Liggieri, L.; Passerone, A. An Automatic Technique for Measuring the Surface Tension of Liquid Metals. *High Temp. Technol.* **1989**, *7*, 82-86.

6.- Sobczak, N.; Singh, M.; Asthana, R. High-Temperature Wettability Measurements in Metal/Ceramic Systems – Some Methodological Issues. *Curr. Opin. Solid. St. M.* **2005**, *9*, 241–253.

7.- Maze, C.; Burnet, G. A Non-Linear Regression Method for Calculating Surface Tension and Contact Angle from the Shape of a Sessile Drop. *Surf. Sci.* **1969**, *13*, 451-470.

8.- http://www.graphensic.com

9.- Ferrari, A.C.; Meyer, J.C.; Scardaci, V.; Casiraghi, C.; Lazzeri, M.; Mauri, F.; Piscanec, S.; Jiang, D.; Novoselov, K. S.; Roth, S.; Geim, A.K. Raman Spectrum of Graphene and Graphene Layers. *Phys. Rev. Lett.* **2006**, *97*, 187401.

10.- Xu, M.; Fujita, D.; Gao, J.; Hanagata, N. Auger Electron Spectroscopy: A Rational Method for Determining Thickness of Graphene Films. *ACS Nano,* **2010**, *4*, 2937-2945.

11.- Emtsev, K.V.; Bostwick, A.; Horn, K.; Jobst, J.; Kellogg, G.L.; Ley, L.; McChesney, J.L.; Ohta, T.; Reshanov, S.A.; *et al*. Towards Wafer-Size Graphene Layers by Atmospheric Pressure Graphitization of Silicon Carbide. *Nat. Mater.* **2009**, *8*, 203-207.

12.- Haydar, S.; Moreno-Castilla, C.; Ferro-García, M.A.; Carrasco-Marín, F.; Rivera-Utrilla, J.; Perrard, A.; Joly, J.P. Regularities in the Temperature-Programmed Desorption Spectra of $CO_2$ and CO from Activated Carbons. *Carbon* **2000**, *38*, 1297-1308.

13.- Caccia, M.; Rodríguez, A.; Narciso, J. Diamond Surface Modification to Enhance Interfacial Thermal Conductivity in Al/Diamond Composites. *JOM,* **2014**, *66*, 920-925.

14.- Thrower, P.A. Chemistry & Physics of Carbon, *Vol. 25*, 1st ed.; CRC Press: Adingdon 1996.

15 Figueiredo, J.L.; Pereira, M.F.R.; Freitas, M.M.A.; Órfao, J.J.M. Modification of the Surface Chemistry of Activated Carbons. *Carbon* **1999**, *37*, 1379-1389.

16.- Rosenthal, D.; Ruta, M.; Schlögl, R.; Kiwi-Minsker, L. Combined XPS and TPD Study of Oxygen-Functionalized Carbon Nanofibers Grown on Sintered Metal Fibers. *Carbon* **2010**, *48*, 1835-1843.

17.- Childres, I.; Jauregui, L.A.; Park, W.; Cao, H.; Chen, Y.P. *New Developments in Photon and Materials Research*, Nova Science Publishers*:* Hauppauge NY 2013**.**

18.- Banhart, F.; Kotakoski, J.; Krasheninnikov, A.V. Structural Defects in Graphene. *ACS Nano* **2010**, *5*, 26-41.